A DECONSTRUCTION OF METHODS TO DERIVE ONE-POINT LENSING STATISTICS

Viviane Alfradique,[1,2]* Tiago Castro,[3,4,5,6]* Valerio Marra,[3,4,7] Miguel Quartin,[1,8,9]
Carlo Giocoli[10,11] and Pierluigi Monaco[3,4,6,12]

[1]Instituto de Física, Universidade Federal do Rio de Janeiro, 21941-972, Rio de Janeiro, RJ, Brazil
[2]Centro Brasileiro de Pesquisas Físicas, Rua Dr. Xavier Sigaud 150, 22290-180 Rio de Janeiro, RJ, Brazil
[3]INAF – Osservatorio Astronomico di Trieste, via Tiepolo 11, I-34131 Trieste, Italy
[4]INFN – Sezione di Trieste, I-34100 Trieste, Italy
[5]IFPU – Institute for Fundamental Physics of the Universe, via Beirut 2, 34151, Trieste, Italy
[6]ICSC - Centro Nazionale di Ricerca in High Performance Computing, Big Data e Quantum Computing, Via Magnanelli 2, Bologna, Italy
[7]Departamento de Física, Universidade Federal do Espírito Santo, 29075-910, Vitória, ES, Brazil
[8]PPGCosmo, Universidade Federal do Espírito Santo, 29075-910, Vitória, ES, Brazil
[9]Observatório do Valongo, Universidade Federal do Rio de Janeiro, 20080-090, Rio de Janeiro, RJ, Brazil
[10]INAF - Osservatorio Astronomico di Bologna, via Piero Gobetti 93/3, I-40129 Bologna, Italy
[11]INFN, Sezione di Bologna, viale Berti Pichat 6/2, I-40127 Bologna, Italy
[12]Università di Trieste, Dipartimento di Fisica, via Tiepolo 11, 34143 Trieste
Version May 2, 2024

ABSTRACT

Gravitational lensing is a crucial tool for exploring cosmic phenomena, providing insights into galaxy clustering, dark matter, and dark energy. Given the substantial computational demands of N-body simulations, approximate methods like PINOCCHIO and turboGL offer viable alternatives for simulating lensing probability density functions (PDFs). This paper evaluates these methods in contexts where baryonic effects are negligible, focusing on dark matter-dominated models and assessing their effectiveness across both weak and strong lensing regimes. Our comparative analysis reveals that these methods are particularly effective for applications involving electromagnetic and gravitational wave point sources, where strong lensing events are infrequent. Both PINOCCHIO and turboGL perform well in modeling the weak-lensing region influenced by mildly nonlinear structures. However, they lose accuracy in capturing small-scale nonlinear matter fields, owing to oversimplified assumptions about internal halo structures and reliance on perturbation theory. The analysis shows that PINOCCHIO achieves an 8–15% agreement with N-body simulations for the second-to-fourth moments of lensing PDFs. These findings aim to inform future studies on gravitational lensing of point sources, which are increasingly relevant with upcoming supernova and gravitational wave datasets.

Keywords: large-scale structure of Universe – cosmology:observations – cosmological parameters

1. INTRODUCTION

Electromagnetic and gravitational wave point sources, such as supernovae and compact binary coalescences, have proven to be invaluable for studying the universe's evolution across extensive redshift ranges. Upcoming observatories like the Euclid mission,[1] the Nancy Grace Roman Space Telescope,[2] and the Vera C. Rubin Observatory[3] are set to accurately observe tens of thousands of supernovae up to a redshift of $z \sim 2$. Simultaneously, third-generation gravitational wave detectors such as the Einstein Telescope[4] and Cosmic Explorer[5] will detect hundreds of thousands of gravitational events up to $z \sim 5$ and beyond. To harness this wealth of data effectively, it is crucial to meticulously model all potential systematic effects, with gravitational lensing being a significant concern, particularly for sources at $z \gtrsim 1$, as it strongly influences distance measurements.

Gravitational lensing affects electromagnetic and gravitational waves as they traverse our inhomogeneous Universe. This phenomenon describes the deflections that waves undergo when interacting with the matter density field, causing distant sources to appear magnified or demagnified. Such deflections can lead to significant distance measurement errors, modifying the intrinsic distribution of astronomical sources and introducing variance and non-Gaussianities. Furthermore, this deflections also gives rise to distortions in the shapes of the background galaxies. A gravitational lens induces a correlation on galaxy image orientations which can be measured statically and reveal the properties and evolution of large-scale structures. This is known as *cosmic shear* (see e.g. Bartelmann and Schneider 2001; Kilbinger 2015, for a review).

Gravitational lensing notably limits the accuracy of distant standard candles and sirens as cosmological probes. Estimates suggest that lensing adds a relative uncertainty of 0.5%–1% to distance measurements of stellar binary black holes up to 3 Gpc (Shan et al. 2021). Recent studies, such as those by Mpetha et al. (2024), have indicated that neglecting this effect can bias cosmological analyses of bright sirens at $z \leq 0.5$ by more than 1σ, resulting in $\Delta H_0 = \pm\, 0.25$ km/s/Mpc for binary neutron stars (BNS) and $\Delta H_0 = \pm\, 5$ km/s/Mpc for supermassive black hole binaries. Canevarolo and Chisari (2023) further demonstrated that gravitational lensing could introduce biases up to 3.5σ for the Ω_{m0} measurement and up to 2.5σ for H_0 using BNS up to $z = 2$, and Canevarolo et al. (2024) that lensing may also bias the distribution of neutron star masses. Moreover, Wu et al. (2023) showed that 'delens-

---

*These authors contributed equally to this work.
[1] https://www.euclid-ec.org/
[2] https://roman.gsfc.nasa.gov/
[3] https://www.lsst.org/
[4] https://www.et-gw.eu
[5] https://cosmicexplorer.org

ing' methods, which correct the effect after estimating the lensing magnification independently through weak lensing maps reconstructed from galaxy surveys, could halve these lensing errors on average (Shapiro et al. 2010).

Accurate modeling of gravitational lensing effects on the Hubble diagram residuals can yield significant cosmological insights. By meticulously addressing the systematic effects of lensing, researchers can effectively transform what appears as noise into a valuable signal. Numerous studies (Quartin et al. 2014; Castro and Quartin 2014; Castro et al. 2016b,a; Macaulay et al. 2017, 2020; Scovacricchi et al. 2017) have investigated the correlation between the Hubble diagram residuals and lensing signals, examining how these relationships depend on the background cosmology and the perturbations in intervening matter. These efforts have demonstrated the potential to achieve a precision of 0.6% for the amplitude of the power spectrum σ_8 and 7% for the growth rate index γ in forthcoming surveys (Amendola et al. 2015).

The lensing probability distribution function (PDF) is the fundamental one-point statistic for describing the lensing of point sources. The most direct and precise method for determining the lensing PDF involves applying the ray-tracing technique in full hydrodynamical cosmological simulations (Castro et al. 2018). However, these simulations demand extensive computational resources. In regimes with negligible baryonic effects on lensing, N-body simulations using collisionless particles provide a sufficient alternative and significantly reduce computational demands. Despite the reliability of the results from N-body simulations (Takahashi et al. 2011; Hilbert et al. 2020), the computational requirements and storage capacities remain challenging.

An even faster approach, which combines precision and speed, is to use approximate methods to describe the nonlinear evolution of perturbations (Manera et al. 2012; Kitaura and S. 2013; Tassev et al. 2013; Monaco 2016). The *PINpointing Orbit Crossing Collapsed HIerarchical Objects* (PINOCCHIO) algorithm (Monaco et al. 2002; Taffoni et al. 2002; Munari et al. 2016) integrates Lagrangian perturbation theory (LPT) with a semi-analytical model to approximate the nonlinear hierarchical formation of structures. This method generates dark matter halo catalogs using a fraction of the resources needed for N-body simulations and achieves roughly 10% accuracy in clustering statistics (power spectrum, bispectrum, and two-point correlation function). For the weak-lensing regime, the stochastic gravitational lensing (sGL) approach provides an even faster alternative (Kainulainen and Marra 2009, 2011a,b). This method calculates the 1-halo term of the lensing PDF using stochastic configurations of inhomogeneities based on a halo model and subsequently incorporates the 2-halo term through convolution. A similar analytical method was recently proposed by Thiele et al. (2020).

In this paper, we deconstruct the essential physics needed to calculate lensing PDFs accurately. We explore the effect of the 2-halo term, the influence of non-collapsed matter in the field, the accuracy of PINOCCHIO, and the degree to which baryonic effects can be overlooked. We specifically analyze four relevant lensing quantities in one-point statistics: the PDFs for convergence (κ), shear (γ), magnification (μ), and magnitude magnification (Δm), the latter being particularly crucial for the statistics of lensing of standard candles like supernovae and gravitational waves. We will describe our methodology in Section 2, present our comparative results in Section 3, and summarize our findings in Section 4. In Appendix A, we revise the impact of the angular resolution on the lensing PDF.

Table 1
Simulation methods ordered according to their complexity and the range of physical phenomena modeled.

model name	description
`tgl` 1h	Stochastic gravitational lensing simulation with the 1-halo turboGL code.
`tgl` 1h+2h	Extends `tgl` 1h by including a theoretical 2-halo term convolution.
PINOCCHIO$_{\text{halos}}$	Ray-tracing on PINOCCHIO past light cone (PLC) with field particles randomly redistributed.
PINOCCHIO	Ray-tracing on standard PINOCCHIO PLC.
N-body	Ray-tracing on N-body simulation PLC.
Hydro	Ray-tracing on hydro-dynamical simulation PLC.

2. LENSING SIMULATION METHODS

This study aims to assess the accuracy of various simulation methods in deriving the lensing Probability Density Function (PDF) on the regime in which baryonic physics is sub-dominant. The methods under investigation are summarized in Table 1, ranked by their complexity and the breadth of physical phenomena they encompass. For the PINOCCHIO and N-body simulations, we further evaluate the angular power spectrum and the generated lensing and density maps. The Hydro simulations are used simply to define the boundaries of reliability of the N-body results. For all methods, our fiducial model for the Universe is the ΛCDM model with the cosmological parameters set very close to the ones obtained by the combination of DES Y1 + Planck 2015 + JLA SNe + BAO (Abbott et al. 2018): $\Omega_{\text{m0}} = 0.301$, $\Omega_{\text{b0}} = 0.048$, $\Omega_{\Lambda 0} = 0.699$, $h = 0.682$, $\sigma_8 = 0.798$, and $n_{\text{s}} = 0.973$. We proceed to describe each method in detail.

2.1. *The sGL method*

The turboGL (`tgl`) code[6] is the numerical implementation of the semi-analytical stochastic gravitational lensing (sGL) method, which was introduced in Kainulainen and Marra (2009, 2011a). The sGL method operates by modeling the matter density contrast according to the halo model (HM), where the inhomogeneous Universe is approximated as a collection of different types of halos whose positions satisfy the linear power spectrum.

2.1.1. *The halo model*

The halo model assumes that on small scales (large wavenumbers k) the statistics of matter correlations are dominated by the internal halo density profiles. In contrast, on large scales, the halos are assumed to cluster according to linear theory. The model does not include intermediate low-density structures such as filaments and walls. Following Kainulainen and Marra (2011b), in `tgl` the total power spectrum is obtained by the simple addition of the two components:[7]

$$P_m(k, z) = P_L(k, z) + P_H(k, z).$$ (1)

The first term on the right-hand side is also called the 2-halo component, and the second is the 1-halo component. The usefulness of the halo model stems from the fact that both terms in Eq. (1) can be computed without having to resort to numerical simulations. Specifically (Peacock and

---

[6] https://github.com/valerio-marra/turboGL
[7] More sophisticated and accurate versions of the HM are available in the literature; see Asgari et al. (2023), and references therein.

Smith 2000):

$$P_L(k,z) = \frac{2\pi^2}{k^3}\delta_{H0}^2 \left(\frac{ck}{H_0}\right)^{3+n_s} T^2(k)D^2(z), \quad (2)$$

$$P_H(k,z) = \int_{M_{\min}}^{\infty} \mathrm{d}n(M,z)\left(\frac{M\,W_k(M,z)}{\rho_{M0}}\right)^2, \quad (3)$$

where $T(k)$ is the transfer function, $D(z)$ the growth function, H_0 is the present-day Hubble parameter, n_s is the spectral index, and δ_{H0} is the amplitude of perturbations on the horizon scale today, which we fix by setting σ_8. Furthermore, in Eq. (3), $M_{\min}$ is the smallest halo mass that is considered, $\mathrm{d}n$ is the number density of halos in the mass range $\mathrm{d}M$, which is defined via the halo mass function $f(M,z)$ that gives the fraction of the total mass in halos of mass M at the redshift z:

$$\mathrm{d}n(M,z) \equiv n(M,z)\mathrm{d}M = \frac{\rho_{M0}}{M}\,f(M,z)\mathrm{d}M, \quad (4)$$

where $n(M,z)$ is the number density and ρ_{M0} the matter density today. Finally, W_k is the Fourier transform of the halo density profile:

$$W_k(M,z) = \frac{1}{M}\int_0^R \rho(r,M,z)\frac{\sin kr}{kr}4\pi\,r^2\,\mathrm{d}r, \quad (5)$$

and R is the halo radius. For the halo profile $\rho(r,M,z)$, we use the Navarro-Frenk-White (NFW) profile (Navarro et al. 1996). Modifications to the inner cuspy NFW profile by baryonic feedback are neglected.

2.1.2. *Lensing convergence*

The lens convergence κ in the Born approximation is given by the following integral evaluated along the unperturbed light path (Bartelmann and Schneider 2001):

$$\kappa(z_s) = \int_0^{r_s} \mathrm{d}r\,\rho_{M0}\,G(r,r_s)\,\delta_M\big(r,t(r)\big), \quad (6)$$

where G is the lensing efficiency of inhomogeneity at the comoving radius r (basically the inverse of the critical surface density defined below):

$$G(r,r_s) = \frac{4\pi G}{c^2 a}\frac{f_k(r)f_k(r_s-r)}{f_k(r_s)}. \quad (7)$$

The functions $a(t)$ and $t(r)$ are the scale factor and geodesic time for the background FLRW model, $r_s = r(z_s)$ is the comoving position of the source at redshift z_s and $f_k(r) = \sin(r\sqrt{k})/\sqrt{k},\ r,\ \sinh(r\sqrt{-k})/\sqrt{-k}$ depending if the curvature $k >,=,< 0$, respectively.

Because in Eq. (6) the contributions to the total convergence are combined additively, it is useful to decompose the density field into a sum of Fourier modes:

$$\delta_M(\boldsymbol{r},t) = \int_0^{\infty}\frac{d^3\boldsymbol{k}}{(2\pi)^3}\,e^{i\boldsymbol{k}\cdot\boldsymbol{r}}\,\delta_M(\boldsymbol{k},t). \quad (8)$$

Eq. (8) can be used to separate the contributions to the convergence due to small-scale inhomogeneities from the ones due to large-scale inhomogeneities so that, similarly to Eq. (1), it is:

$$\kappa(z) = \kappa_L(z) + \kappa_H(z). \quad (9)$$

2.1.3. *2-halo convergence PDF*

Given Eqs. (2), (6) and (8), it is straightforward to obtain the variance of the convergence PDF:

$$\sigma_{\kappa_L}^2 = \int_0^{r_s}\mathrm{d}r\rho_{M0}^2 G^2(r,r_s)\int_0^{k_L}\frac{k\,\mathrm{d}k}{2\pi}P_L\big(k,z(r)\big). \quad (10)$$

The third moment (skewness) can be obtained via the bispectrum (three-point correlation function), which should also contribute to the variance (although the contribution is expected to be small at these linear scales). Here, we take an alternative approach and model the full PDF relative to the 2-halo term as a log-normal distribution with zero mean and the variance given by Eq. (10), see Marra et al. (2013) for details. This is motivated by the well-known fact that the lensing PDF inherits the log-normal character of the density contrast PDF.

In Eq. (10), the cut-off scale k_L separates the 2-halo contribution, characteristic of larger scales, from the 1-halo term, relevant at smaller scales. The precise determination of k_L is theoretically challenging, especially because, at a given redshift, the dependence on the halo masses is nontrivial. Consequently, we employ a pragmatic approach to establish this scale, which involves adjusting it so that the lensing PDF derived from `tgl` matches that obtained from `PINOCCHIO`$_{\text{halos}}$. A detailed description of the method involving `PINOCCHIO`$_{\text{halos}}$ is provided in Section 2.3. The latter's matter field representation closely matches indeed the one used by `tgl`, making it a suitable reference for this calibration. We determined that $k_L = \exp(3.9-4.6z)$ Mpc^{-1} achieves a good agreement, showing that k_L increases at lower redshifts. This aligns with the fact that the halo model does not represent low-density filamentary structures, which become relatively more important at lower redshifts. Addressing this discrepancy necessitates the inclusion of higher mode wavenumbers in calculating the 2-halo variance, thereby compensating for the model's lack of power in these regions.

2.1.4. *1-halo convergence PDF*

The contribution to the convergence from the 1-halo term could be similarly computed via the halo power spectrum:

$$\sigma_{\kappa_H}^2 = \int_0^{r_s}\mathrm{d}r\rho_{M0}^2 G^2(r,r_s)\int_{k_H}^{k_{\max}}\frac{k\,dk}{2\pi}P_H\big(k,z(r)\big), \quad (11)$$

where $k_{\max}$ is the cut-off to account for the finite angular resolution. The other cut-off scale k_H is instead relative to the size of the halos: for $k \ll k_H$, halos contribute to Eq. (11) only via shot noise.

Thanks to the sGL method, we can improve upon the previous result and obtain an estimate equivalent to including the information from all the n-point correlation functions. As explained in Kainulainen and Marra (2011a), the halo contribution to Eq. (6) can be rewritten as:

$$\kappa_H = \sum_{i,u}\kappa_{1iu}(z_s)\Big(k_{iu}-\Delta N_{iu}\Big), \quad (12)$$

where κ_{1iu} is the convergence due to one object in the bin iu:

$$\kappa_{1iu}(z_s) \equiv G_i(r_s)\,\Sigma_{iu}(t_i), \quad (13)$$

where Σ_{iu} is the surface mass density of the halo in the bin iu. Here, the index i labels the lens planes, while the index u labels the parameters that define the surface density; for halos these are the impact parameter and the halo mass. Now, as far as the 1-halo term is concerned, the integers k_{iu} are distributed as Poisson random variables:

$$P_{k_{iu}} = \frac{(\Delta N_{iu})^{k_{iu}}}{k_{iu}!}\,e^{-\Delta N_{iu}}, \quad (14)$$

where the parameter ΔN_{iu} is the expected number of objects in the bin volume ΔV_{iu}:

$$\Delta N_{iu} = \Delta n_{iu}\,\Delta V_{iu} = \Delta n_{iu}\,\Delta r_i\,\Delta A_{iu}, \quad (15)$$

where Δn_{iu} is the comoving density of objects corresponding to the parameters in the bin iu, Δr_i is the bin in the geodesic path, and ΔA_{iu} is the corresponding cross-sectional area of the halos in co-moving units.

From Eq. (12), using the properties of the Poissonian distribution, one can see that $\langle \kappa_H \rangle = 0$ and (Kainulainen and Marra 2011a,b):

$$\sigma_{\kappa_H}^2 = \sum_{i,u} \kappa_{1iu}^2 \, \Delta N_{iu} \,, \tag{16}$$

$$\mu_{3,\kappa_H} = \sum_{i,u} \kappa_{1iu}^3 \, \Delta N_{iu} \,, \tag{17}$$

from which, going back to integral form, one obtains:

$$\sigma_{\kappa_H}^2 = \frac{1}{N_O} \int_0^{r_s} dr \, G^2(r, r_s) \int_{M_{\min}}^{\infty} dn(M, z(r))$$
$$\times \int_0^{R(M,z(r))} dA(b, M) \, \Sigma^2(b, M, z(r))) \,, \tag{18}$$

$$\mu_{3,\kappa_H} = \frac{1}{N_O} \int_0^{r_s} dr \, G^2(r, r_s) \int_{M_{\min}}^{\infty} dn(M, z(r))$$
$$\times \int_0^{R(M,z(r))} dA(b, M) \, \Sigma^3(b, M, z(r)) \,. \tag{19}$$

The integral limits for the last two integrals are implicitly defined, $dA(b) \equiv 2\pi b \, db$ and Σ is the halo surface density:

$$\Sigma(b, M, z) = a^3 \int_b^R \frac{2 \, r \, dr}{\sqrt{r^2 - b^2}} \, \rho(r, M, z) \,. \tag{20}$$

Again, we want to point out that these expressions use the halo profiles in real space and not in Fourier space, thus including higher-order correlation terms beyond the power spectrum.

Obtaining the moments beyond μ_3 analytically is more challenging as there is no closed form. It is easier to estimate them by drawing a set of Poissonian numbers k_{iu}, from which the full convergence PDF and its moments can be easily estimated.

2.1.5. *Full convergence PDF*

The full convergence PDF is finally obtained by convolving the 1- and 2-halo PDFs. The former is obtained via a histogram of a (Poissonian) realization; the latter is based on the log-normal template previously discussed. The final PDF is in the image plane.

The 1-halo contribution is based on binning the comoving space around the photon geodesic. We adopt a fine enough binning such that the numerical results converge. Furthermore, we smooth the NFW density profile via a Gaussian kernel in order to have a fixed angular resolution. The PDF will then be relative to this corresponding smoothing angular resolution, as is the case for the other methods adopted in this study. Finally, the modeling of the halos follows the prescription adopted in PINOCCHIO; that is, we adopt the mass function by Watson et al. (2013, Eq. 12, FOF) and the concentration parameter model by Bhattacharya et al. (2013, 200_c). Furthermore, the smallest halo we model ($M_{\min}$ in the previous equations) has a mass that corresponds to the minimum halo mass adopted in the PINOCCHIO simulations, that is, $2.6 \times 10^9 h^{-1} M_\odot$ (10 dark matter particles, see Table 2).

2.2. *Light-cone construction and ray tracing*

The past light cone (PLC) lens maps for the PINOCCHIO and N-body simulations were constructed using the SLICER[8] code (Castro 2024), introduced in Castro et al.

[8] https://github.com/TiagoBsCastro/SLICER

Table 2
Basic properties from the simulations used in this work. From left to right: the size of the box, gravitational softening, number of DM particles and their masses, the number of lens planes built up to $z = 5$, the field of view of the constructed past light-cone, and the number of PLC realizations (different random seeds).

$L_{\rm box}$ (Mpc/h)	$\epsilon_{\rm soften.}$ (kpc/h)	$N_{\rm part.}$	$m_{\rm DM}$ $(M_\odot/h)$	$N_{\rm planes}$ ($z \le 5$)	FoV (deg.)	PLCs
150	1.4	1024^3	2.6×10^8	118	1.0	20

(2018).[9] This code distributes particles within the light cone based on the simulation snapshots. The process begins with SLICER configuring the field of view and setting the maximum source redshift, as specified in the input file. Subsequently, the code determines the required number of lens planes to ensure a continuous construction of the light cone. Each simulation snapshot is then processed sequentially. The code reads the files, selecting particles within the predetermined field of view. Prior to projecting these particles onto the lens plane, each snapshot undergoes a randomization process. This step involves reflecting and translating the center of the particle distribution, in accordance with the periodic boundary conditions. Additionally, a specific face of the simulation cube is chosen to align with the line of sight. The final stage involves constructing the lens planes. This is achieved by mapping the positions of particles to the nearest preselected lens plane. The angular positions of the particles are maintained during this process. The surface density is then pixelated using the triangular cloud method, as described in Hockney and Eastwood (1988) and Bartelmann (2003). The grid pixels are carefully selected to maintain a consistent angular size across all planes. To prevent repetition of cosmic structures in the field of view (FoV) and to ensure that the map sizes are equivalent to the simulation box size (set at 150 Mpc/h), all maps are constructed with a uniform FoV value of 1°, see Table 2. Consequently, using SLICER, we successfully generated 20 light cones up to $z_s = 5$. These cones comprise 118 lens maps with varying resolutions: 2048^2, 1024^2, 512^2, and 256^2 pixels. These resolutions correspond to angular resolutions of 1.76, 3.52, 7.03, and 14.06 arcsec, respectively.

After creating the lens planes, the lensing quantities (convergence κ, shear γ, and magnification μ) are computed using the ray-tracing technique, which integrates the non-linear matter on the unperturbed trajectory of the source plane to the observer. Castro et al. (2018) showed that the latter Born approximation yields accurate results for 1-point lensing statistics. In the thin lens approximation, i.e., disregarding the size of each lens, the convergence for a single lens plane is

$$\kappa(\boldsymbol{\theta}) = \frac{\Sigma(\boldsymbol{\theta})}{\Sigma_{\rm crit}}, \tag{21}$$

where $\boldsymbol{\theta}$ is the observed angular position, $\Sigma(\boldsymbol{\theta})$ is the surface mass density and $\Sigma_{\rm crit}$ is the critical surface density

$$\Sigma_{\rm crit} = \frac{c^2 D_l}{4\pi G D_s D_{ls}}. \tag{22}$$

In the above, c is the speed of light, G is the gravitational constant, D_l, D_s and D_{ls} are the angular diameter distances between the observer-lens, observer-source, and lens-source, respectively. Thus, we use equation (21) to obtain the differential convergence maps, which are summed up to the source redshift.

The shear maps were computed using the Shear Map

[9] SLICER is an improved and fully rewritten version of MapSim (Giocoli et al. 2015).

Reconstruction (SMR) `PYTHON` script distributed with `SLICER`. The shear components γ_1, γ_2 are written as a function of the deflection potential Ψ:

$$\gamma_1(\boldsymbol{\theta}) = \frac{1}{2}(\Psi_{\theta_1\theta_1} - \Psi_{\theta_2\theta_2}), \qquad (23)$$

$$\gamma_2(\boldsymbol{\theta}) = \Psi_{\theta_1\theta_2} = \Psi_{\theta_2\theta_1}, \qquad (24)$$

where

$$\Psi(\boldsymbol{\theta}) = \frac{1}{\pi}\int \kappa(\boldsymbol{\theta}')\ln|\boldsymbol{\theta} - \boldsymbol{\theta}'|\,\mathrm{d}^2\theta'. \qquad (25)$$

SMR uses FFTW to reconstruct the lensing potential from the convergence maps and fourth-order finite differences to calculate its shear components.

Finally, the magnification μ is computed using the relation

$$\mu \equiv \frac{1}{(1-\kappa)^2 - \gamma^2}, \qquad (26)$$

where $\gamma = \sqrt{\gamma_1^2 + \gamma_2^2}$ is the shear modulus. In the weak lensing regime, the above relation is reduced to

$$\mu \approx 1 + 2\kappa + \gamma^2 + 3\kappa^2. \qquad (27)$$

We computed the angular power spectra P_κ and P_γ for all the convergence and shear maps, respectively. In linear theory, it is $P_\kappa = P_\gamma$, and for a source at z_s it is written as an integral of the density contrast along the unperturbed path of light, using the Limber approximation (Limber 1953; Munshi et al. 2008; Bartelmann and Schneider 2001):

$$P_\kappa(l, z_s) = \frac{9H_0^4\Omega_{\mathrm{m}0}^2}{4c^4}\int_0^{\chi_s}\mathrm{d}\chi'\left(\frac{\chi_s - \chi'}{\chi_s\,a(\chi')}\right)^2 P_m\left(\frac{l}{\chi'}, \chi'\right), \qquad (28)$$

where $\chi(z)$ is the comoving distance at z, $\chi_s = \chi(z_s)$, and P_m is the linear matter power-spectrum.

2.3. *PINOCCHIO*

`PINOCCHIO` generates simulated halo catalogs using the ellipsoidal collapse to compute the collapse time, defined as the moment of orbit crossing, and Lagrangian perturbation theory (LPT) to displace the formed halos and uncollapsed particles. Briefly, `PINOCCHIO` works as follows: a linear field is smoothed using a Gaussian filter at various scales, the collapse time is calculated for each particle (grid point) with the ellipsoidal collapse; these are then sorted by collapse time in chronological order and displaced according to the LPT theory; later, the code groups the collapsed particles into halos and filaments in order to properly reproduce the hierarchical formation of the structures; and finally the LPT theory is used to move the halos to their final position and thus describe their evolution. As the particles that are members of a halo have passed through orbit crossing, their displacements are extrapolations of the LPT displacement outside its validity; therefore, `PINOCCHIO` cannot provide reliable profiles needed for accurate lensing statistics. The particles belonging to halos are then redistributed assuming a NFW profile and the mass-concentration relation given by Bhattacharya et al. (2013, 200_c).

We use `PINOCCHIO` configured in the third order of the LPT theory to build a set of simulations defined according to Table 2. In an effort to better compare `PINOCCHIO` and sGL results, we consider two `PINOCCHIO` configurations (see Table 1): i) the label `PINOCCHIO` represents the complete results (halos+filaments+uncollapsed particles that do not belong to any structure) of the standard `PINOCCHIO` code, and ii) the label `PINOCCHIO`$_{\mathrm{halos}}$ considers only the halos and randomizes the rest.

As a note, the construction of a lightcone from snapshots is an inefficient use of `PINOCCHIO`, because the code itself

Table 3
Ranges where the PDFs from the Hydro and DM versions of Magneticum Box 3 hr differ by less than 50% (1.76 arcsec).

Statistics	Redshift	Range
Convergence	1	$[-\infty, 0.38]$
Convergence	2	$[-0.12, 0.50]$
Convergence	3	$[-0.17, 0.50]$
Convergence	5	$[-0.25, 0.49]$
Shear	1	$[1.1 \times 10^{-5}, 5.8 \times 10^{-2}]$
Shear	2	$[2.3 \times 10^{-5}, 1.3 \times 10^{-1}]$
Shear	3	$[5.5 \times 10^{-5}, 1.5 \times 10^{-1}]$
Shear	5	$[6.0 \times 10^{-5}, 1.9 \times 10^{-1}]$
Magnification	1	$[0.93, 2.3]$
Magnification	2	$[0.88, 3.2]$
Magnification	3	$[0.83, 2.4]$
Magnification	5	$[0.72, 2.9]$
Magnitude	1	$[-0.90, 0.08]$
Magnitude	2	$[-1.26, 0.14]$
Magnitude	3	$[-0.95, 0.20]$
Magnitude	5	$[-1.16, 0.36]$

outputs halos in a lightcone, and the position of particles outside halos can be easily recovered at any time using LPT. However, in this study, we prefer to apply to the `PINOCCHIO` runs the same analysis applied to the N-body simulations.

2.4. *N-body simulations*

The N-body simulations used in this work were performed using the GADGET-2 code (Springel 2005), following the configurations described in Table 2. The GADGET-2 code uses the parallelized Tree–Particle Mesh (TreePM, see Xu 1995) algorithm to calculate the gravitational interactions between the simulation particles. In this algorithm, these interactions are separated into a long-range term, calculated using the Particle-Mesh methods, and a short-range term for interactions of close neighbors that are described via the Tree algorithm (Barnes and Hut 1986).

The simulations contain only collisionless matter accounting for the amount of cold dark matter and baryons, excluding any effect of baryonic feedback. The dark matter particles were evolved from $z = 99$ to $z = 0$ in a comoving box with a side equal to 150 Mpc/h and mass resolution of $2.6 \times 10^8\,M_\odot/h$ (see Table 2). The choice for this box size is justified by the fact that it has already been shown in Castro et al. (2018) that a box of 128 Mpc/h with a mass resolution of $10^8\,M_\odot/h$ is enough to obtain convergent results for the lensing PDF.

2.5. *Hydrodynamical simulations*

The effect of baryons on lensing probability density functions and the convergence power spectrum $P_\kappa(\ell)$ was thoroughly examined by Castro et al. (2018) using hydrodynamic simulations. This study specifically analyzed the multipole range of $P_\kappa(\ell)$ and the value ranges for κ, γ, and μ across various redshifts, identifying thresholds below which the baryonic contributions are minimal. Given the challenges associated with extracting cosmological information in scenarios where baryonic effects—such as AGN and stellar feedback, star formation, magnetic fields, and thermal conduction—are significant, our analysis adopts a simplified approach. We thus avoid the complexities of expensive hydrodynamical simulations by focusing on the dark matter-dominated regime, ensuring that baryonic effects remain below the 50% threshold. Although more
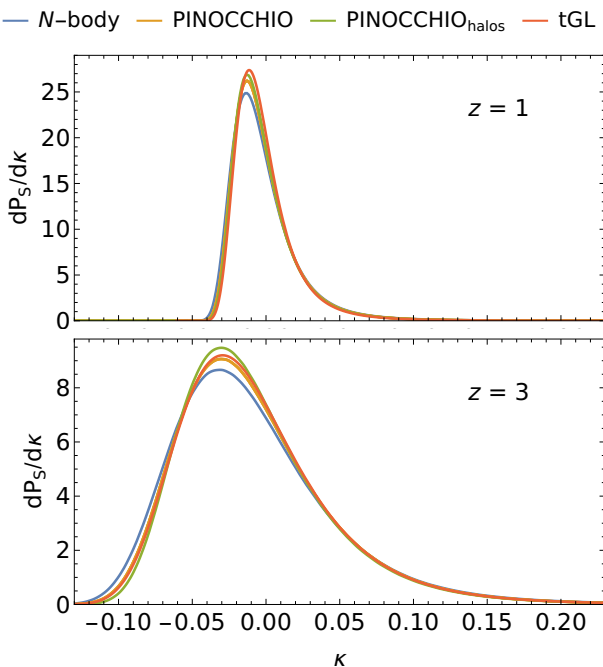
Figure 1. Convergence PDFs for the different lensing methods considered in this study, for an angular resolution of 1.76 arcsec.

stringent thresholds could be employed, it is pertinent to note that for many lensing statistics, like the moments of the PDFs (Marra et al. 2013), the discrepancies between DM-only and baryonic cases are minimal, as our DM model effectively captures the bulk of the distributions.

Table 3 displays the ranges within which the PDFs from the Hydro and DM versions of Box 3 (hr) of the Magneticum simulation suite[10] differ by less than 50%, given a resolution of 1.76 arcsec. To avoid overcrowding in the plots, only the ranges corresponding to redshifts $z = 1$ and $z = 3$ will be presented.

3. RESULTS

We now present our results for the PDFs of convergence, shear, magnification, and magnitude. In the ray-tracing method employed, rays are calculated from the source to the observer, resulting in statistics computed in the image plane. In most cases, we subsequently translate these PDFs to the source plane, which is relevant to observations. Hereafter, the PDFs in the image and source planes are denoted by the subscripts I and S, respectively.

As detailed in Castro et al. (2018), the lensing PDFs intrinsically depend on the angular resolution. This dependency is not directly related to the point spread function of any particular telescope, but rather to the angular scale used for computing averages. For example, for a fixed lens and source position, the average magnification of galaxies with diameters of 1 and 5 arcsec may differ. As discussed in Section 2.5, our simulations yield reliable results for a minimal angular resolution of 1.76 arcsec, which we adopt as our fiducial resolution for most discussions. However, results for lower resolutions are presented in Appendix A.

3.1. Lensing PDFs

In Fig. 1, we display the κ PDFs derived using the three different methods considered in this study: full N-body simulations, PINOCCHIO (including the 'halos' variant), and the stochastic turboGL code, as described in Section 2 and

---

[10] http://www.magneticum.org

summarized in Table 1. These are depicted for $z = 1$ and $z = 3$ at our fiducial angular resolution of 1.76 arcsec. The methods generally exhibit good agreement, particularly in the peak position. However, the N-body simulations show a slightly larger variance, as indicated by the lower PDF peak and normalization condition. Since these plots probe weak convergences and, therefore, mildly nonlinear structures, the slight discrepancies should be attributed to a lack of modeling precision at the scale of filaments, which will be discussed subsequently.

However, differences in the tails of the distributions are obscured by the linear scale used in Fig. 1. Therefore, in Fig. 2, we present a general comparison between the results from N-body and PINOCCHIO for κ, γ, and μ on a logarithmic scale, depicting four different redshifts for each method. The turboGL code is excluded from this comparison as it does not compute the shear PDFs so that μ can be inferred only in the weak-lensing regime. As previously discussed, our analysis focuses on the region where baryonic effects are maintained below the 50% level. The regimes where this is not the case at $z = 1$ and $z = 3$ are highlighted with a blue and green shade, respectively. It is evident that as the source distance increases, the convergence, shear, and magnification PDFs become wider (indicating higher variance), and the peaks of their distributions shift (indicating skewness). We will further explore these trends for convergence in Section 3.3, noting the general trend that lensing intensifies at higher redshifts due to the increased number of lens encounters. We find that both PINOCCHIO and N-body simulations are consistent with the theoretical model of randomly distributed point-mass lenses (Schneider et al. 1992), which predicts that when $\gamma < 0.01$, the PDF is proportional to γ^2, and for $\mu \gg 1$, the PDF is proportional to μ^{-1}. However, while the asymptotic behavior prediction of the randomly distributed points model for the $\gamma-$PDF happens within the range where the baryonic effects are subdominant, the prediction for the $\mu-$PDF occurs in the regime deeply dominated by baryonic physics and is not shown in Fig. 2. The behavior of the magnification PDF at this regime will be discussed in Sect. 3.2.

Figure 3 illustrates the differences between the PDFs from PINOCCHIO and turboGL compared to the N-body results. Both approximate methods exhibit a small excess of probability density at the peak of the distribution and a deficiency in the tail. These discrepancies stem from the limitations of the approximate methods in accurately reproducing the non-linear density field, likely due to an inadequate representation of substructures and halo concentrations which are prevalent in this non-linear regime and responsible for high-convergence events. We find that PINOCCHIO provides a better approximation than the stochastic method at $z = 1$, but both methods perform comparably at $z = 3$. However, both methods gradually fail for larger κ, exhibiting approximately 20% discrepancies for $\kappa \geq 0.2$, which falls well within the DM-dominated regime. Moreover, the lower the redshift, the smaller the κ value at which this breakdown occurs. Interestingly, for the shear, we observe much better agreement between PINOCCHIO and N-body in the region of interest. Differences become apparent at $\gamma \gtrsim 0.1$, a region dominated by baryonic effects. An explanation for this disagreement will be proposed in Section 3.5. For the $\mu-$PDFs, we again observe that as we venture into more non-linear regimes, specifically for $\mu > 2$, notable differences emerge between both methods. However, these differences are proportionally smaller in the DM-dominated regime than in the case of κ. Particularly, the agreement is consistently good for $\mu < 1$—where the PDF rapidly decreases, causing relative
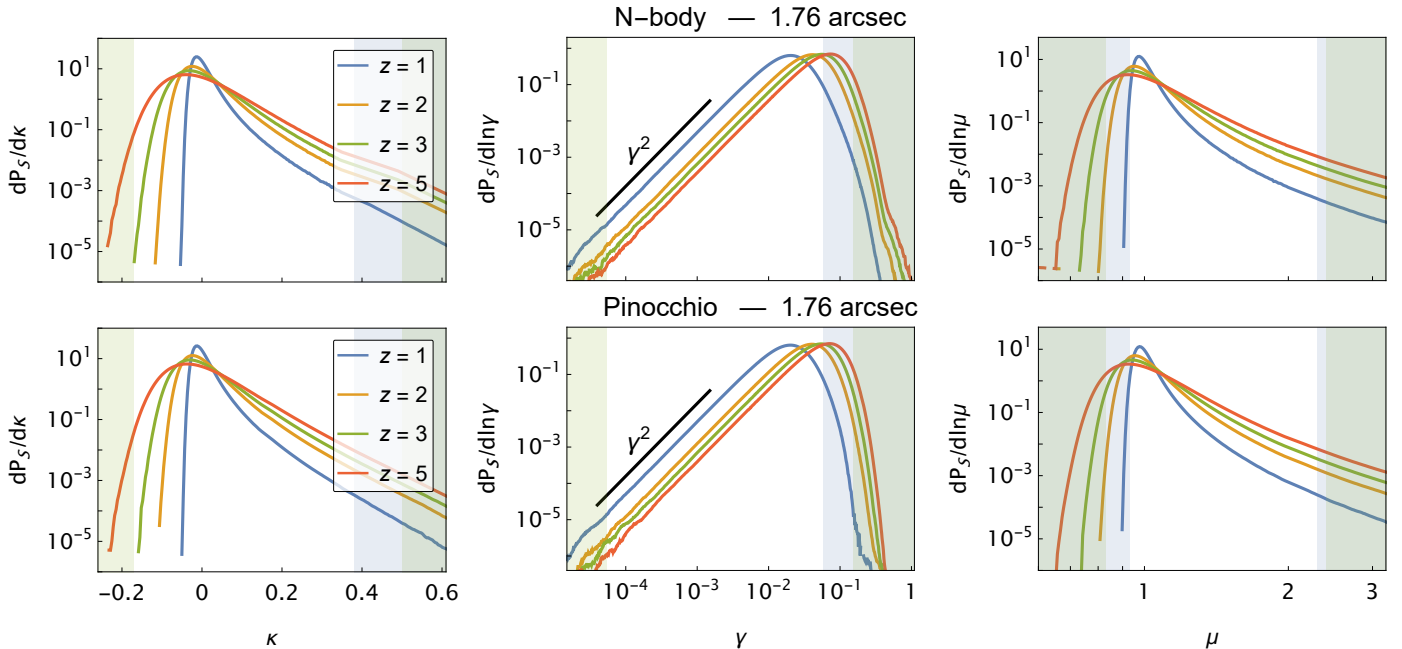
Figure 2. Comparison of κ, γ and μ PDFs (in the source plane) for different redshifts for the N-body and PINOCCHIO case for the angular resolution of 1.76 arcsec. PINOCCHIO$_{halos}$ (not shown here for compactness) exhibit similar behavior to PINOCCHIO. The shaded regions mark where baryonic corrections exceed 50% for $z = 1$ (blue) or for $z = 3$ (green). As can be seen the two methods agree reasonably well in the range where baryonic effects are under control. See also Fig. 3.
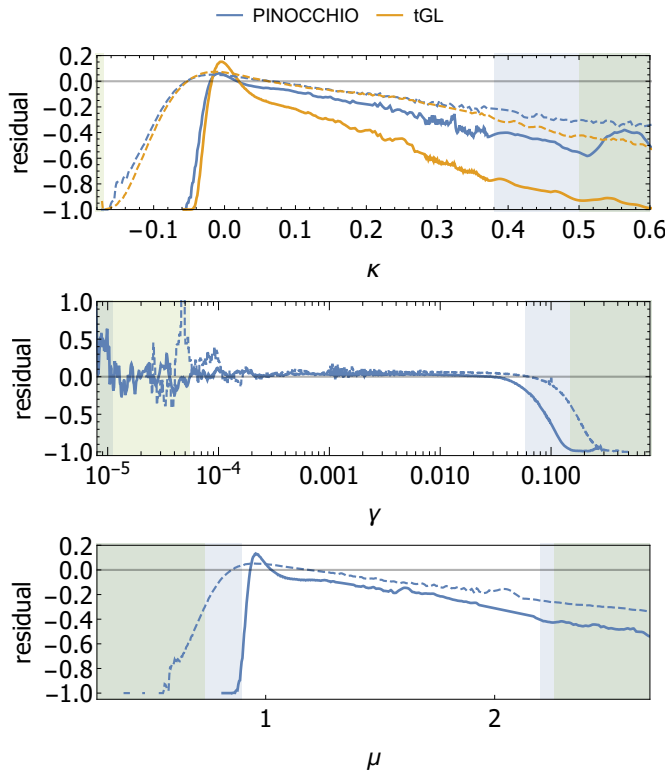

Figure 3. Relative residual differences between approximate methods and the full N-body results in the source plane, for $z = 1$ (solid lines) and $z = 3$ (dashed lines). The blue (green) shaded regions represent the interval in which the baryonic correction is over 50% for $z = 1$ ($z = 3$).

residuals to increase—and ranges between 20% and 40% for larger μ until baryonic physics becomes dominant. As we will explore later, the multiple-image regime begins beyond these baryonic thresholds; thus, only the so-called type-I μ-PDF is relevant here (see, e.g., Takahashi et al. 2011; Castro et al. 2018). A similar comparison for different angular resolutions is presented in Appendix A.

3.2. Strong lensing PDFs

Here, we present the lensing PDFs in the strong-lensing regime, computed by differentiating contributions from various image types defined as follows:

$$\text{Type I:} \quad |1 - \kappa| > \gamma \quad \text{and} \quad \kappa < 1,$$
$$\text{Type II:} \quad |1 - \kappa| < \gamma,$$
$$\text{Type III:} \quad |1 - \kappa| > \gamma \quad \text{and} \quad \kappa > 1. \tag{29}$$

Type II and III images indicate the strong-lensing regime, characterized by multiple images (Schneider et al. 1992), while Type I involves only image amplification.

Figure 4 displays the PDFs of κ, γ, and μ for $z = 5$, categorized into these three types. We see that the N-body simulations show a higher probability of forming Types II and III images compared to structures generated by the PINOCCHIO code, highlighting the limitations of the method in accurately describing the strong-lensing regime (in the present implementation the halo internal structure is described by a single spherical NFW profile without substructure). The absence of most Type II and III images in PINOCCHIO is also consistent with observations from the previous section that the PINOCCHIO PDFs disagree from the N-body results for $\gamma \gtrsim 0.1$. Furthermore, we find that the angular resolution does not significantly impact the lensing PDFs in the strong-lensing regime, and comparisons between the PINOCCHIO and PINOCCHIO$_{halos}$ PDFs show nearly indistinguishable results, with the exception of the Type II κ PDFs.

Additionally, we corroborate several findings from Castro et al. (2018):

- The magnification PDFs from the N-body simulations indicate that the observed plateau in the demagnification region results from Type II images.

- The emergence of secondary peaks in the high shear region is due to the transition from Type I to Types II and III.

- The plateau in the high-convergence tail of the convergence PDFs, starting at $\kappa \sim 1$, stems from the presence of Type III images.
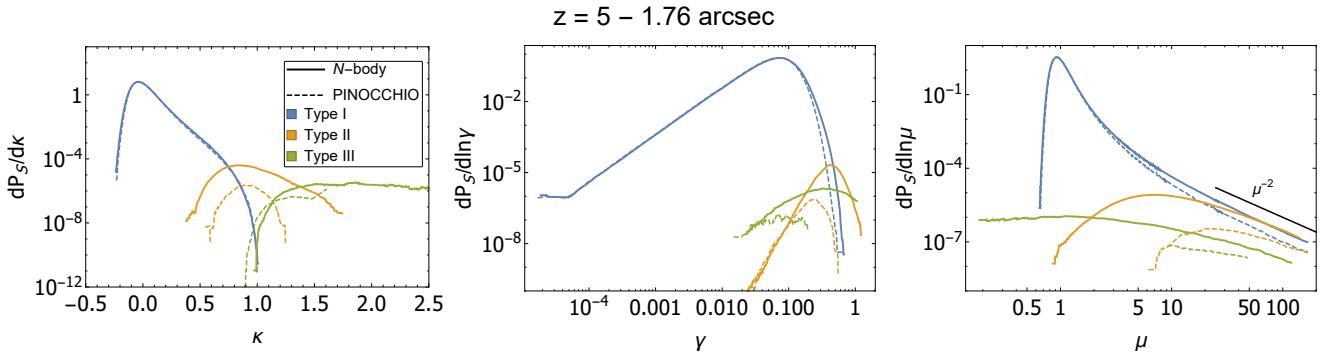
Figure 4. Convergence, shear and magnification PDFs at $z = 5$ for different angular resolutions for the different image types.
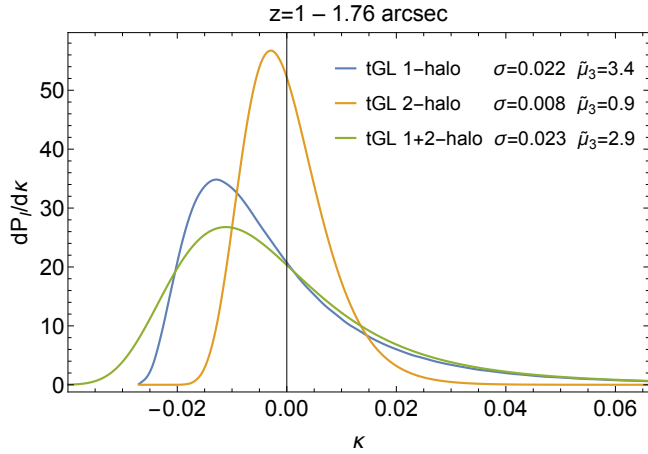

Figure 5. Image-plane convergence PDFs relative to the 1-halo and 2-halo contributions together with the full PDF obtained by convolving the previous two. One can see that the 1-halo contribution is more significant than the 2-halo one.

3.3. Dissecting the PDF

Figure 5 shows the halo-model convergence PDF from `turboGL` together with the individual contributions from the 1- and 2-halo terms. We can see that the total lensing variance is dominated, as expected, by the 1-halo contribution and that the log-normal template features a mild skewness $\tilde{\mu}_3 = \mu_3/\sigma^3$ (the third standardized moment).

Next, we show, breaking the sums of Eqs. (16) and (17) into individual elements, the contributions to the variance μ_2 and skewness $\tilde{\mu}_3$ of halos with a given mass (Fig. 6) and in a given lensing plane redshift (Fig. 7), for sources at $z = 1$ and $z = 3$. It is also shown the average number of lensing-halo hits per light ray. In the case of Fig. 7, a value of 10 in a given Δz, for instance, means that the light ray hit on average 10 halos in that redshift bin (bin widths are constant in comoving distance), and similarly for Fig. 6.

From Fig. 6 (top panel) we can see that our simulations consider the relevant range of masses as the halos with mass $\approx 10^{13} h^{-1} M_\odot$ contribute to most of the variance, and halos with masses below $10^9 h^{-1} M_\odot$ or above $10^{15} h^{-1} M_\odot$ have a negligible impact. Also, the lensing PDF for sources at $z = 3$ has a variance which is about 5 times greater than the PDF for sources at $z = 1$ – the light ray encounters more lenses in the former case. Regarding skewness, we observe that more massive halos contribute significantly to the overall asymmetry of the PDF. This is due to less massive halos being more numerous, thereby distributing the same fraction of the Universe's mass across a greater number of objects. Consequently, a ray experiences a higher number of interactions (hits). According to the central limit theorem, this results in a PDF that more closely approximates a Gaussian distribution. Finally, a
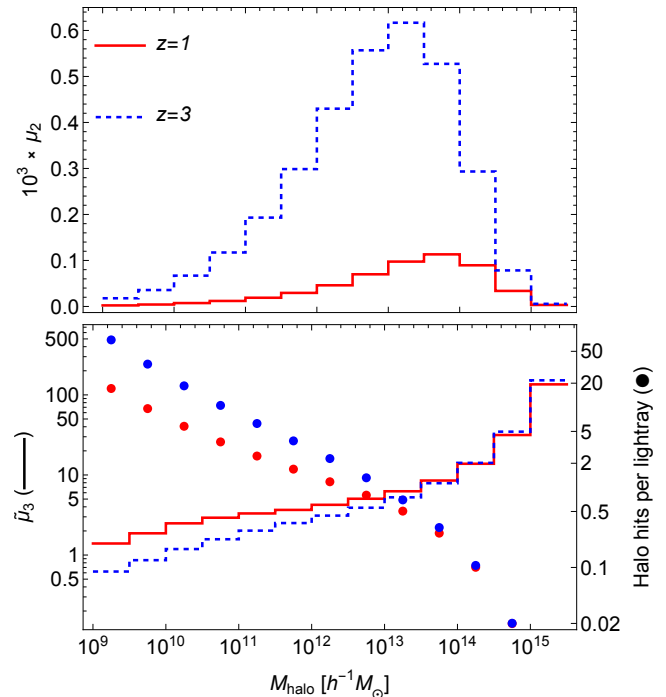

Figure 6. Contribution to the variance μ_2 (top) and skewness $\tilde{\mu}_3 = \mu_3/\sigma^3$ (bottom) of lensing halos with a given mass for sources at $z = 1$ and $z = 3$ using Eqs. (16)–(17). Also shown (point markers) is the average number of lensing-halo hits per light ray. See Section 3.3.

source at $z = 3$ is further away, and a larger number of halos are encountered so that the number of hits is larger and the skewness is lower. At the very high-mass end, the skewness for sources at $z = 3$ is slighter higher because the extra number of hits with respect to $z = 1$ does not compensate for the very skewed distributions of those very massive halos.

The top panel of Fig. 7 shows the contributions of the lens planes to the variance. The shape is modulated by the lensing efficiency of Eq. (7) and the growth of structures. The largest contributions come at about half way between source and observer. The bottom panel shows the contribution to the skewness. The overall trend is that lens planes at lower redshifts contribute to a higher skewness. From Fig. 6, we remember that smaller halos have a smaller number of hits at lower redshifts (and produce relatively more skewness), while this is the opposite for larger halos. The overall effect is dominated by the smaller halos, which can be attributed to the progressive nonlinearity in the Universe due to the growth of structures. We also see that the contributions for different source redshifts are exactly one on top of the other. It is useful to remember that the skewness in the matter and lensing distributions is due to the fact that under-densities occupy more volume than
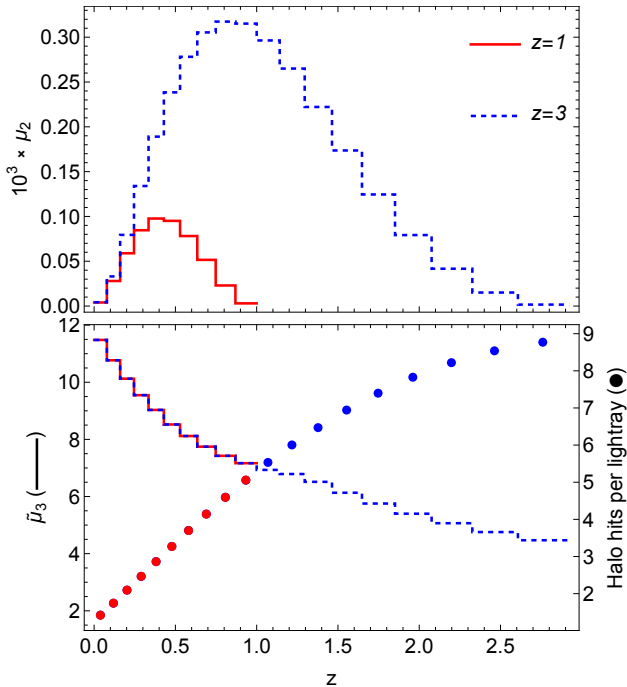
Figure 7. Contribution to the variance (top) and skewness (bottom) of halos of a given lensing plane redshift for sources at $z = 1$ and $z = 3$ using Eqs. (16)-(17). Also shown (point markers) is the average number of lensing-halo hits per light ray. See Section 3.3.

overdensities, so it is more likely to encounter an underdensity or have a de-magnified light beam. Therefore, the third standardized moment is only due to geometry and does not depend on the lensing efficiency of Eq. (7), which depends on the source redshift.

3.4. Momenta of the magnitude PDF

We now focus on analyzing the second, third, and fourth central moments of the shift in magnitude Δm, which directly relates to magnification μ through:

$$\Delta m \equiv 2.5 \log_{10} \mu. \tag{30}$$

Using magnitudes is advantageous because the magnitude PDF exhibits more stable central moments than the μ–PDF, which has a divergent variance in cosmology. Nevertheless, truncating the magnitude PDF at a certain negative Δm value is prudent, as highly magnified objects could, in principle, be individually detected and excluded from the statistics either *a posteriori* or during target selection *a priori*.[11] Furthermore, as previously demonstrated, the baryonic contribution becomes dominant for $\mu \gtrsim 3$, which is outside the focus of this study.

Results for redshifts 1 and 3, computed in the source plane with a fixed angular resolution of 1.76 arcsec, are depicted in Fig. 8. These PDFs are assessed up to a cutoff magnitude, Δm_{cut}, beyond which the PDF is considered zero. The second central moment shows the strongest agreement, indicating PINOCCHIO's capability to accurately reproduce the body rather than the tail of the PDF distribution – a consistency noted in earlier sections. Particularly, at $z = 3$, PINOCCHIO and PINOCCHIO$_{halos}$ agree more closely with N-body results compared to $z = 1$, except for $\mu_{2,lens}$ in PINOCCHIO$_{halos}$. We interpret the latter disagreement as due to the higher relative importance of non-halo particles at higher redshifts, at which halos give a less complete description of the matter field (see next

[11] These methods accurately recover the mean of the non-truncated PDFs, which is essential for unbiased cosmological analyses. Since the mean is a non-central moment, we will not discuss here the effects of truncation on it.
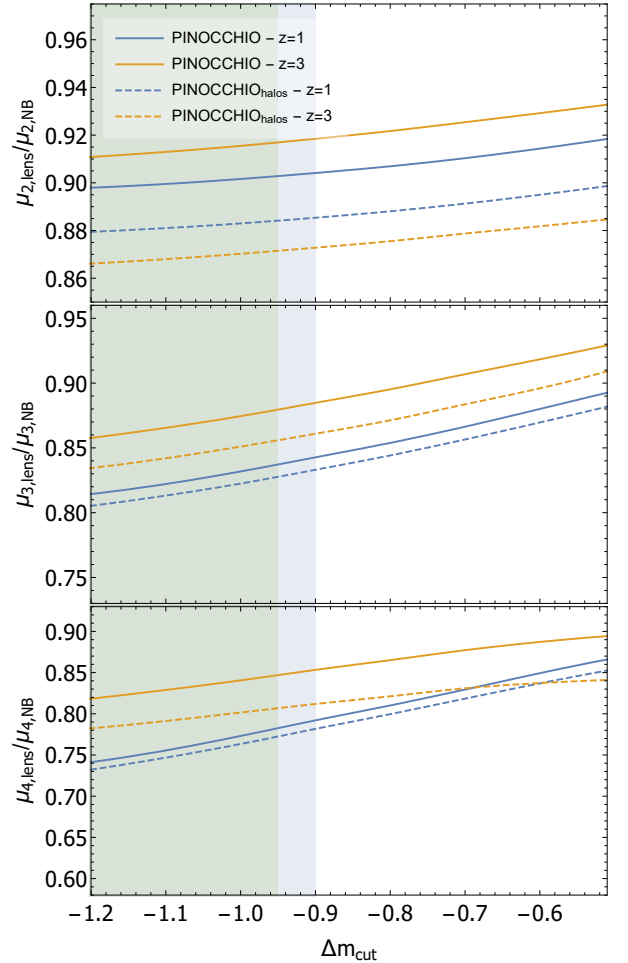

Figure 8. Central moments' ratio of the magnitude PDFs of the approximative methods with respect to the N-body simulation, for different values of Δm_{cut} and for $z = 1$ and $z = 3$. The blue (green) shaded regions indicate the limit where the baryonic effects is dominant, above 50%, for $z = 1$ ($z = 3$).

section). This indicates that non-halo particles have a significant impact on the central moments, suggesting that the discrepancies with the N-body results are not simply due to the halo profiles and positioning.

Overall, PINOCCHIO well models statistical quantities within limits where baryonic effects are negligible. This precision makes it a useful tool for constructing simple models of central moments as functions of redshift and cosmological parameters. These models are crucial for the MeMo method (Quartin et al. 2014), which utilizes the weak lensing effect on the intrinsic distribution of magnitudes to constrain key cosmological parameters, such as the amplitude of the matter power spectrum and the matter density parameter (Quartin et al. 2014; Castro and Quartin 2014; Castro et al. 2016a).

3.5. Maps and power spectrum

Finally, to gain a deeper understanding of our findings, we will analyze the maps of the lensing quantities that underpin the PDFs discussed in previous sections, along with the convergence power spectra generated by the PINOCCHIO code and the N-body simulations across various redshifts.

In Fig. 9, we display the projected density maps of matter distributed over the lens plane at redshifts $z = 1$ and $z = 3$, reconstructed using the N-body simulations and PINOCCHIO in its two configurations. These maps highlight the distribution of halos and filaments, as well as the presence of galaxy clusters at the intersections of filaments. We observe a better agreement between PINOCCHIO
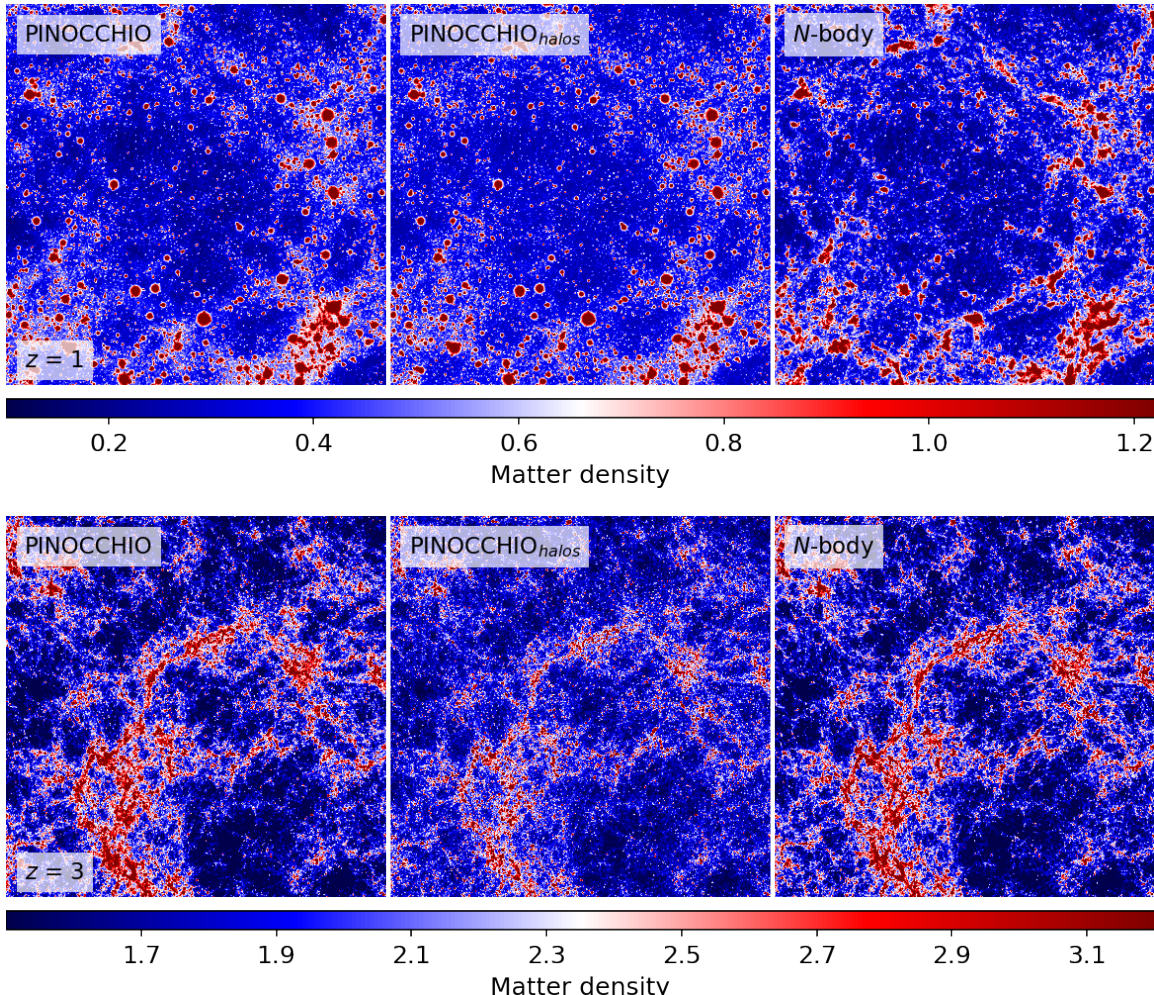
Figure 9. Projected density maps for the angular resolution of 1.76 arcsec. The projected slice has a thickness of 150 Mpc/h.

and N-body at $z = 3$, with PINOCCHIO$_{halos}$ showing weaker structures. This is consistent with our previous observation that non-halo particles become more significant at higher redshifts, where the simulated halos provide a less comprehensive depiction of the matter field. Indeed, the absence of halos smaller than those defined by the mass resolution of the simulation leads to a relatively greater importance of diffuse matter between halos, responsible for power on large-scale modes crucial for replicating the linear distribution of structures. Conversely, while PINOCCHIO and PINOCCHIO$_{halos}$ agree well at $z = 1$, their correspondence with the N-body simulation worsens, as halo profiles and positions do not accurately replicate the small-scale patterns observed in the N-body simulations. These results also highlight the limitations of the LPT approximation up to the 3rd order, employed in the PINOCCHIO code, in capturing the distribution of matter on smaller scales. Notably, the absence of more massive structures, which are evident in the N-body simulation maps, confirms this limitation, aligning with findings from early works on the PINOCCHIO code (Monaco 2016; Munari et al. 2017).

The convergence maps and power spectra for the N-body and PINOCCHIO simulations are displayed in Fig. 10. The PINOCCHIO maps begin to diverge from those of the N-body simulations at small scales, yet show good agreement on larger scales. This observation is corroborated both through visual inspection and by analyzing the angular convergence power spectrum, which shows a 1–2σ consistency for $l \lesssim 10^4$, consistent with the observations from Fig. 9. At small scales, the contribution of the halo profile becomes dominant, where the lack of substructures

in the profile adopted here implies the disagreement observed in this limit.[12] Additionally, Fig. 11 presents a comparison of the shear maps. There is broad agreement between the maps for both $z = 1$ and $z = 3$. Distinctions between PINOCCHIO, PINOCCHIO$_{halos}$, and the N-body simulations become noticeable only at high-shear levels. Here, the filaments represented in PINOCCHIO appear more pronounced than those in the N-body simulation, highlighting the limits of agreement. This finding is consistent with the analysis of the PDFs detailed in Sections 3.1 and 3.2, which highlighted disagreement for $\gamma \gtrsim 0.1$. In particular, we can infer that the correct modeling of filaments is important for type II and III images.

4. CONCLUSIONS

In this paper, we investigated the effectiveness of the approximate methods PINOCCHIO and turboGL in accurately reproducing lensing probability density functions (PDFs). Our simulations assume a universe composed solely of dark matter, excluding baryonic effects. We studied the impact of gravitational lensing in both weak and strong regimes, differentiating the contributions from the three types of images. We thoroughly compared the results of these approximate methods with those obtained from N-body simulations. Key findings include:

1. Approximate methods are effective primarily within the weak and medium-lensing region, which mainly

---

[12] See Giocoli et al. (2017) for the effects of substructures in the power spectrum and PDFs.
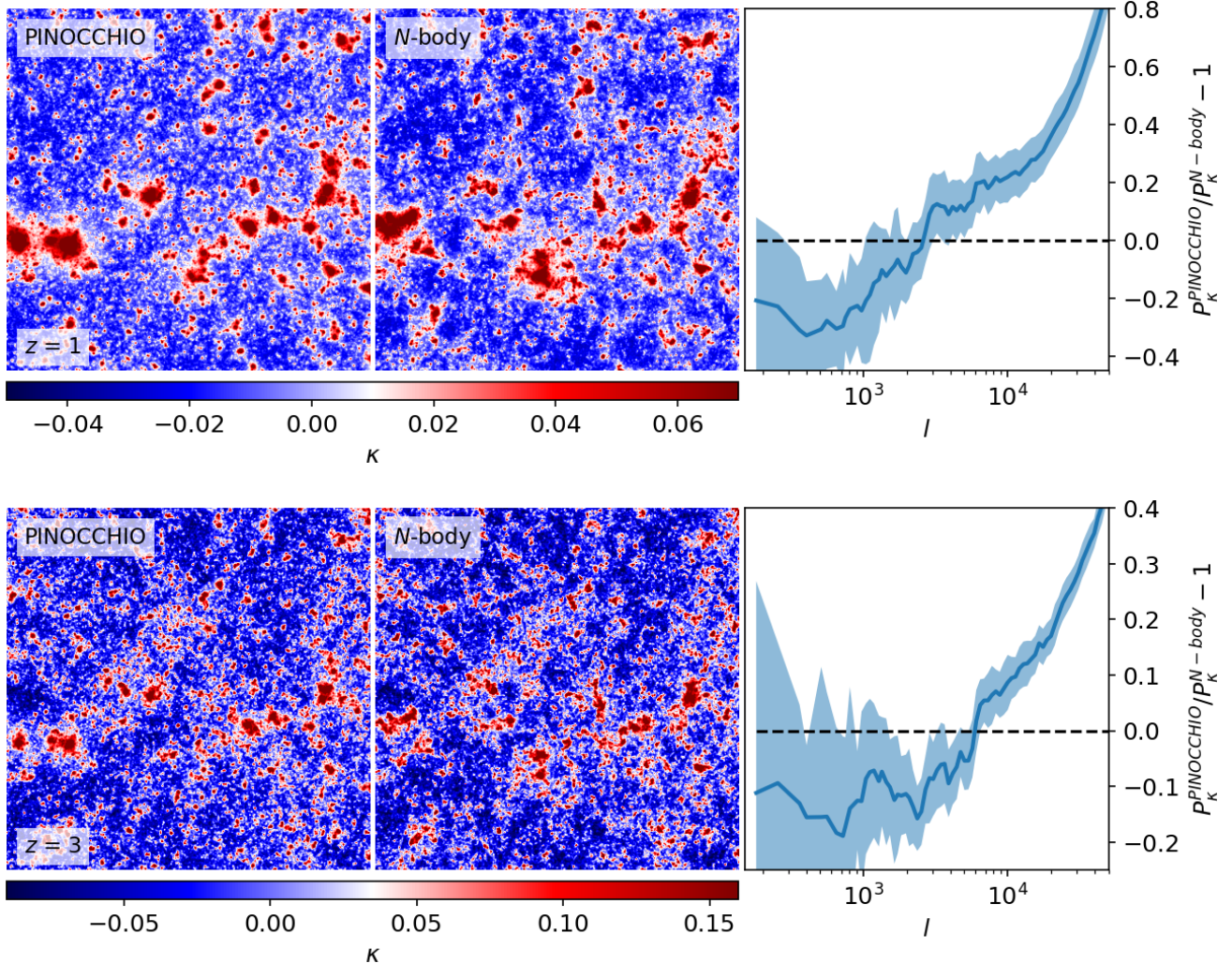
Figure 10. Comparison of convergence maps and angular power spectra for the angular resolution of 1.76 arcsec. The displayed ratio represents the average across 20 PLCs, with error bands reflecting the propagated uncertainties of this average.

arises from mildly nonlinear matter structures. Accurately modeling the tails of the PDFs necessitates N-body simulations, as demonstrated by our analysis of Types I, II, and III lensing PDFs.

2. For supernovae and standard sirens these methods prove useful for statistical analyses, given that strong lensing events are either rare or can be excluded. Within this regime, baryonic effects are expected to have a minor impact.

3. These approximate methods struggle to accurately capture the small-scale nonlinear matter field. As the perturbation theory fails to accurately predict small-scale halo clustering and intertwining matter distribution, enhancing the modeling of halo internal structures could improve results. Recent work by Berner et al. (2022) has initiated efforts to reconstruct halo substructure from merger histories, which could be integrated into these methods to add more small-scale power to the simulations. We also observed that non-halo particles minimally impact lensing for $z < 3$.

4. Our evaluation of the second-to-fourth moments of the lensing PDFs indicated that `PINOCCHIO` agrees with N-body results to within 8–15% in regimes where baryonic effects are minimal.

5. The stochastic simulations of `turboGL` are suitable for rapid likelihood exploration due to their speed

and flexibility in handling low-statistics PDFs ($\sim 10^5$ rays). In contrast, ray tracing is more effective at exploring high-μ tails as the number of rays increases with the square of the field of view, while stochastic methods scale linearly with sample size.

6. The analyses of the moments in Figs. 6 and 7 and the maps (Figs. 9–11) underscore the need for precise modeling of mass distribution and non-linear clustering of halos with $M > 10^{12} M_\odot$. The challenges are twofold: (i) while there is a moderate consensus on the impact of baryons at the scale of galaxy clusters, their effects in individual galaxies and galaxy groups remain far less understood and more uncertainties (see, e.g., Euclid Collaboration: Castro, T., et al. 2023); (ii) lighter objects in filaments require both accurate modeling of their individual profiles and a detailed understanding of their interconnected mass distributions.

These insights are expected to guide future studies on gravitational lensing of point sources, a topic of growing relevance in light of upcoming supernova and gravitational wave datasets.

Figure 11. Shear maps for the angular resolution of 1.76 arcsec.

DATA AND SOFTWARE AVAILABILITY

Codes will be shared on reasonable request to the corresponding author. Data products and post-processing routines are available at (Castro et al. 2024).[13]

REFERENCES

Abbott T. M. C., et al. (2018) Dark Energy Survey year 1 results: Cosmological constraints from galaxy clustering and weak lensing. *Phys. Rev. D*, 98(4):043526, DOI 10.1103/PhysRevD.98.043526, 1708.01530

Amendola L., Castro T., Marra V., Quartin M. (2015) Constraining the growth of perturbations with lensing of supernovae. *MNRAS*, 449:2845–2852, DOI 10.1093/mnras/stv497, URL https://academic.oup.com/mnras/article/449/3/2845/2892989, 1412.3703

Asgari M., Mead A. J., Heymans C. (2023) The halo model for cosmology: a pedagogical review. DOI 10.21105/astro.2303.08752, 2303.08752

Barnes J., Hut P. (1986) A Hierarchical 0 Nlogn Force Calculation Algorithm. *Nature*, 324:446–449, DOI 10.1038/324446a0

Bartelmann M. (2003) Numerical methods in gravitational lensing. *ArXiv e-prints*, astro-ph/0304162

Bartelmann M., Schneider P. (2001) Weak gravitational lensing. *Phys. Rep.*, 340:291–472, DOI 10.1016/S0370-1573(00)00082-X, URL https://doi.org/10.1016/S0370-1573(00)00082-X, 9912508

Berner P., Refregier A., Sgier R., Kacprzak T., Tortorelli L., Monaco P. (2022) Rapid simulations of halo and subhalo clustering. *JCAP*, 11:002, DOI 10.1088/1475-7516/2022/11/002, 2112.08389

Bhattacharya S., Habib S., Heitmann K., Vikhlinin A. (2013) Dark Matter Halo Profiles of Massive Clusters: Theory versus Observations. *ApJ*, 766(1):32, DOI 10.1088/0004-637X/766/1/32, 1112.5479

Canevarolo S., Chisari N. E. (2023) Lensing bias on cosmological parameters from bright standard sirens. 2310.12764

Canevarolo S., van Vonderen L., Chisari N. E. (2024) Impact of lensing of gravitational waves on the observed distribution of neutron star masses. 2404.11480

Castro T. (2024) Tiagobscastro/slicer: v2.0.1. DOI 10.5281/zenodo.11048430, URL https://doi.org/10.5281/zenodo.11048430

Castro T., Quartin M. (2014) First measurement of σ_8 using supernova magnitudes only. *Mon. Not. Roy. Astron. Soc.*, 443:L6, DOI 10.1093/mnrasl/slu071, 1403.0293

[13] github.com/TiagoBsCastro/LensingMethodsDeconstruction

Castro T., Marra V., Quartin M. (2016a) Constraining the halo mass function with observations. *Mon.Not.Roy.Astron.Soc.*, 463:1666–1677, DOI 10.1093/mnras/stw2072, 1605.07548

Castro T., Quartin M., Benitez-Herrera S. (2016b) Turning noise into signal: learning from the scatter in the Hubble diagram. *Phys. Dark Univ.*, 13:66–76, DOI 10.1016/j.dark.2016.04.006, 1511.08695

Castro T., Quartin M., Giocoli C., Borgani S., Dolag K. (2018) The effect of baryons in the cosmological lensing PDFs. *MNRAS*, 478:1305–1325, DOI 10.1093/mnras/sty1117, URL https://doi.org/10.1093/mnras/sty1117, 1711.10017

Castro T., Marra V., Quartin M., Alfradique V. (2024) Tiagobscastro/lensingmethodsdeconstruction: v1.0.1. DOI 10.5281/zenodo.11093020, URL https://doi.org/10.5281/zenodo.11093020

Euclid Collaboration: Castro, T., et al. (2023) Euclid preparation. XXXIX. The effect of baryons on the Halo Mass Function. 2311.01465

Giocoli C., Metcalf R. B., Baldi M., Meneghetti M., Moscardini L., Petkova M. (2015) Disentangling dark sector models using weak lensing statistics. *Mon. Not. Roy. Astron. Soc.*, 452(3):2757–2772, DOI 10.1093/mnras/stv1473, 1502.03442

Giocoli C., Di Meo S., Meneghetti M., Jullo E., de la Torre S., Moscardini L., Baldi M., Mazzotta P., et al. (2017) Fast weak-lensing simulations with halo model. *Mon. Not. Roy. Astron. Soc.*, 470(3):3574–3590, DOI 10.1093/mnras/stx1399, 1701.02739

Hilbert S., Barreira A., Fabbian G., Fosalba P., Giocoli C., Bose S., Calabrese M., Carbone C., et al. (2020) The accuracy of weak lensing simulations. *MNRAS*, 493:305–319, DOI 10.1093/mnras/staa281, URL https://doi.org/10.1093/mnras/staa281, 1910.10625

Hockney R. W., Eastwood J. W. (1988) Computer simulation using particles. CRC Press

Kainulainen K., Marra V. (2009) New stochastic approach to cumulative weak lensing. *Phys. Rev. D*, 80:123020, DOI 10.1103/PhysRevD.80.123020", URL https://doi.org/10.1103/PhysRevD.80.123020, 0909.0822

Kainulainen K., Marra V. (2011a) Accurate modeling of weak lensing with the stochastic gravitational lensing method. *Phys. Rev. D*, 83:023009, DOI 10.1103/PhysRevD.83.023009, URL https://doi.org/10.1103/PhysRevD.83.023009, 1011.0732

Kainulainen K., Marra V. (2011b) Weak lensing observables in the halo model. *Phys. Rev. D*, 84:063004, DOI 10.1103/PhysRevD.84.063004, URL https://doi.org/10.1103/PhysRevD.84.063004, 1101.4143

Kilbinger M. (2015) Cosmology with cosmic shear observations: a review. *Rept. Prog. Phys.*, 78:086901, DOI 10.1088/0034-4885/78/8/086901, 1411.0115

Kitaura F.-S., S. H. (2013) Cosmological structure formation with augmented Lagrangian perturbation theory. *Mon. Not. R. Astron. Soc.: Lett.*, 435:L78–L82, DOI 10.1093/mnrasl/slt101, URL https://doi.org/10.1093/mnrasl/slt101, 1212.3514

Limber D. N. (1953) The Analysis of Counts of the Extragalactic Nebulae in Terms of a Fluctuating Density Field. *ApJ*, 117:134, DOI 10.1086/145672, URL https://articles.adsabs.harvard.edu/pdf/1953ApJ...117..134L

Macaulay E., Davis T. M., Scovacricchi D., Bacon D., Collett T. E., Nichol R. C. (2017) The effects of velocities and lensing on moments of the Hubble diagram. *Mon. Not. Roy. Astron. Soc.*, 467(1):259–272, DOI 10.1093/mnras/stw3339, 1607.03966

Macaulay E., et al. (2020) Weak Lensing of Type Ia Supernovae from the Dark Energy Survey. *Mon. Not. Roy. Astron. Soc.*, 496(3):4051–4059, DOI 10.1093/mnras/staa1852, 2007.07956

Manera M., Scoccimarro R., Percival W. J., Samushia L., McBride C. K., Ross A. J., Sheth R. K., White M., et al. (2012) The clustering of galaxies in the SDSS-III Baryon Oscillation Spectroscopic Survey: a large sample of mock galaxy catalogues. *MNRAS*, 428:1036–1054, DOI 10.1093/mnras/sts084, URL https://doi.org/10.1093/mnras/sts084, 1203.6609

Marra V., Quartin M., Amendola L. (2013) Accurate weak lensing of standard candles. I. Flexible cosmological fits. *Phys. Rev. D*, 88:063004, DOI 10.1103/PhysRevD.88.063004, 1304.7689

Monaco P. (2016) Approximate methods for the generation of dark matter halo catalogs in the age of precision cosmology. *Galaxies*, 4(4):53, DOI 10.3390/galaxies4040053, 1605.07752

Monaco P., Theuns T., G. T. (2002) The PINOCCHIO algorithm: pinpointing orbit-crossing collapsed hierarchical objects in a linear density field. *MNRAS*, 331:587–608, DOI 10.1046/j.1365-8711.2002.05162.x, URL https://doi.org/10.1046/j.1365-8711.2002.05162.x, 0109323

Mpetha C. T., Congedo G., Taylor A., Hendry M. A. (2024) Impact of weak lensing on bright standard siren analyses. *ArXiv e-prints*, DOI 10.48550/arXiv.2402.19476, URL https://arxiv.org/abs/2402.19476, 2402.19476

Munari E., Monaco P., Sefusatti E., Castorina E., Mohammad F. G., Anselmi S., Borgani S. (2016) Improving fast generation of halo catalogues with higher order Lagrangian perturbation theory. *MNRAS*, 465:4658–4677, DOI 10.1093/mnras/stw3085, URL https://doi.org/10.1093/mnras/stw3085, 1605.04788

Munari E., Monaco P., Koda J., Kitaura F.-S., Sefusatti E., Borgani S. (2017) Testing approximate predictions of displacements of cosmological dark matter halos. *JCAP*, 07:050, DOI 10.1088/1475-7516/2017/07/050, URL https://doi.org/10.1088/1475-7516/2017/07/050, 1704.00920

Munshi D., Valageas P., van Waerbeke L., Heavens A. (2008) Cosmology with weak lensing surveys. *Phys. Rep.*, 462:67–121, DOI 10.1016/j.physrep.2008.02.003, URL https://doi.org/10.1016/j.physrep.2008.02.003, 0612667

Navarro J. F., Frenk C. S., White S. D. M. (1996) The Structure of cold dark matter halos. *Astrophys. J.*, 462:563–575, DOI 10.1086/177173, astro-ph/9508025

Peacock J. A., Smith R. E. (2000) Halo occupation numbers and galaxy bias. *Mon. Not. Roy. Astron. Soc.*, 318:1144, DOI 10.1046/j.1365-8711.2000.03779.x, astro-ph/0005010

Quartin M., Marra V., Amendola L. (2014) Accurate weak lensing of standard candles. II. Measuring σ_8 with supernovae. *Phys. Rev. D*, 89:023009, DOI 10.1103/PhysRevD.89.023009, URL https://journals.aps.org/prd/abstract/10.1103/PhysRevD.89.023009, 1307.1155

Schneider P., Ehlers J., Falco E. E. (1992) Gravitational Lenses. Springer Berlin, DOI 10.1007/978-3-662-03758-4

Scovacricchi D., Nichol R. C., Macaulay E., Bacon D. (2017) Measuring weak lensing correlations of Type Ia Supernovae. *Mon. Not. Roy. Astron. Soc.*, 465(3):2862–2872, DOI 10.1093/mnras/stw2878, 1611.01315

Shan X., Wei C., Hu B. (2021) Lensing magnification: gravitational waves from coalescing stellar-mass binary black holes . *MNRAS*, 508:1253–1261, DOI 10.1093/mnras/stab2567, URL https://doi.org/10.1093/mnras/stab2567

Shapiro C., Bacon D. J., Hendry M., Hoyle B. (2010) Delensing gravitational wave standard sirens with shear and flexion maps. *MNRAS*, 404:858–866, DOI 10.1111/j.1365-2966.2010.16317.x, URL https://doi.org/10.1111/j.1365-2966.2010.16317.x

Springel V. (2005) The cosmological simulation code GADGET-2. *MNRAS*, 364:1105–1134, DOI 10.1111/j.1365-2966.2005.09655.x, URL https://doi.org/10.1111/j.1365-2966.2005.09655.x, 0505010

Taffoni G., Monaco P., Theuns T. (2002) PINOCCHIO and the hierarchical build-up of dark matter haloes. *MNRAS*, 333:623–632, DOI 10.1046/j.1365-8711.2002.05441.x, URL https://doi.org/10.1046/j.1365-8711.2002.05441.x, 0109324

Takahashi R., Oguri M., Sato M., Hamana T. (2011) Probability distribution functions of cosmological lensing: convergence, shear, and magnification. *ApJ*, 742:15, DOI 10.1088/0004-637X/742/1/15, URL https://doi.org/10.1088/0004-637X/742/1/15, 1106.3823

Tassev S., Zaldarriaga M., Eisenstein D. (2013) Solving large scale structure in ten easy steps with COLA. *JCAP*, 06:036, DOI 10.1088/1475-7516/2013/06/036, URL https://iopscience.iop.org/article/10.1088/1475-7516/2013/06/036, 1301.0322

Thiele L., Hill J. C., Smith K. M. (2020) Accurate analytic model for the weak lensing convergence one-point probability distribution function and its autocovariance. *Phys. Rev. D*, 102(12):123545, DOI 10.1103/PhysRevD.102.123545, 2009.06547

Watson W. A., Iliev I. T., D'Aloisio A., Knebe A., Shapiro P. R., Yepes G. (2013) The halo mass function through the cosmic ages. *MNRAS*, 433(2):1230–1245, DOI 10.1093/mnras/stt791, 1212.0095

Wu Z. F., Chan L. W. L., Hendry M., Hannuksela O. A. (2023) Reducing the impact of weak-lensing errors on gravitational-wave standard sirens. *MNRAS*, 522:4059–4077, DOI 10.1093/mnras/stad1194, URL https://doi.org/10.1093/mnras/stad1194

Xu G.-H. (1995) A new parallel N body gravity solver: TPM. *Astrophys. J. Suppl.*, 98:355, DOI 10.1086/192166, astro-ph/9409021

APPENDIX

A. PDFS AT DIFFERENT ANGULAR RESOLUTIONS

Figure 12 illustrates how changes in angular resolution affect the lensing PDFs from PINOCCHIO and N-body simu-lations. Increasing the angular resolution angle alters the peak and variance of the lensing PDFs in the following
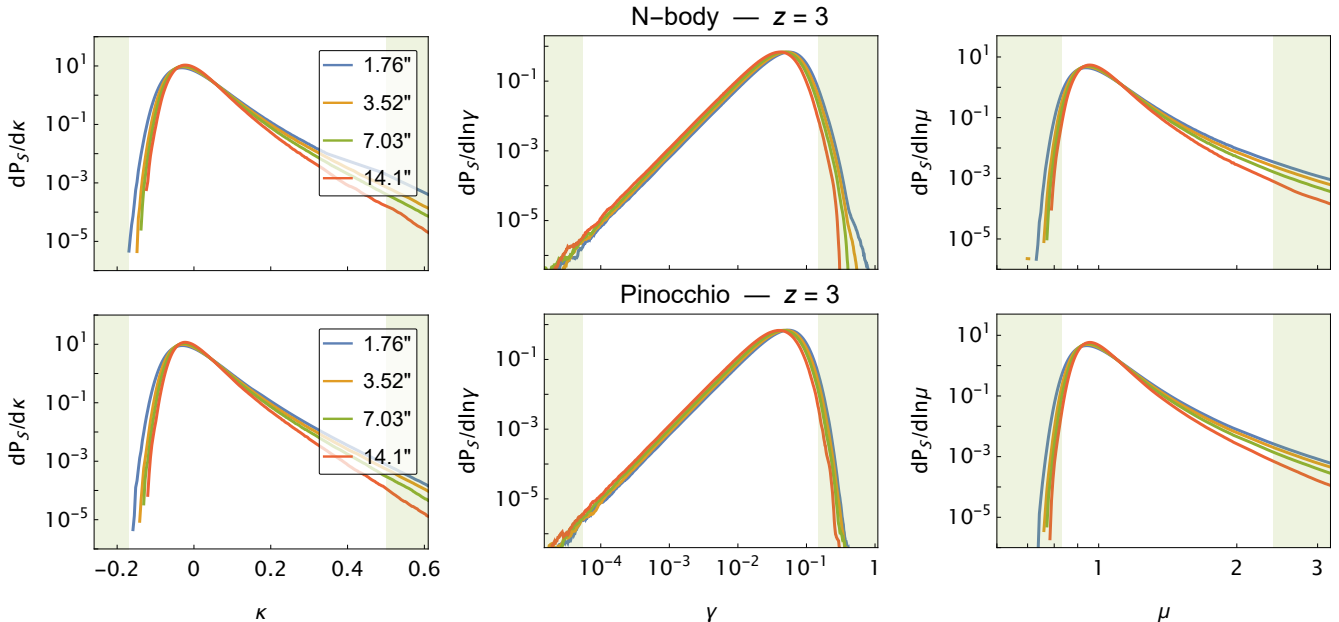
Figure 12. Similar to Figure 2, but for different angular resolutions at $z = 3$. We use the 1.76" resolution as reference for the shaded regions.

ways:

i) the convergence peak shifts to lower $|\kappa|$ values and the variance decreases;

ii) the shear peak shifts to lower γ values without a noticeable change in its variance;

iii) the magnification exhibits a combined effect of i) and ii), where the peak shifts towards $\mu = 1$ and the variance decreases.

This behavior is anticipated as using a larger resolution angle effectively smooths the matter field, thus reducing the overall lensing effect. Notably, the characteristic elbow at $\gamma \gtrsim 0.1$ vanishes with a larger resolution angle. As discussed in Section 3.2, this feature is linked to type II and III images, which are suppressed by the effective smoothing of the matter field.